Hadron masses and baryonic scales in G$_2$-QCD at finite density

Björn H. Wellegehausen[*]

Institut für Theoretische Physik, Justus-Liebig-Universität Giessen, 35392 Giessen, Germany and
Theoretisch-Physikalisches Institut, Friedrich-Schiller-Universität Jena, 07743 Jena, Germany

Axel Maas[†] and Andreas Wipf[‡]

Theoretisch-Physikalisches Institut, Friedrich-Schiller-Universität Jena, 07743 Jena, Germany

Lorenz von Smekal[§]

Institut für Theoretische Physik, Justus-Liebig-Universität Giessen, 35392 Giessen, Germany and
Theoriezentrum, Institut für Kernphysik, Technische Universität Darmstadt, 64289 Darmstadt, Germany

The QCD phase diagram at densities relevant to neutron stars remains elusive, mainly due to the fermion-sign problem. At the same time, a plethora of possible phases has been predicted in models. Meanwhile G$_2$-QCD, for which the $SU(3)$ gauge group of QCD is replaced by the exceptional Lie group G$_2$, does not have a sign problem and can be simulated at such densities using standard lattice techniques. It thus provides benchmarks to models and functional continuum methods, and it serves to unravel the nature of possible phases of strongly interacting matter at high densities. Instrumental in understanding these phases is that G$_2$-QCD has fermionic baryons, and that it can therefore sustain a baryonic Fermi surface. Because the baryon spectrum of G$_2$-QCD also contains bosonic diquark and probably other more exotic states, it is important to understand this spectrum before one can disentangle the corresponding contributions to the baryon density. Here we present a first systematic classification of this spectrum. The qualitative features of this spectrum are reflected in our simulation results at different quark masses although our lattices are still rather coarse. This allows us to relate the mass hierarchy, ranging from scalar would-be-Goldstone bosons and intermediate vector bosons to the G$_2$ nucleons and deltas, to individual structures observed in the total baryon density at finite chemical potential.

I. INTRODUCTION

Understanding neutron stars requires understanding the equilibrium properties of nuclear and hadronic matter [1,2] at low temperature and high density. This is essential in every stage, starting from neutron star formation and cooling to neutron star mergers, and hence ultimately to understanding the synthesis of the heavy elements. A serious technical obstacle in this process is the infamous fermion-sign problem, which prevents efficient numerical simulations of the underlying theory of nuclei and hadrons, QCD [3–5]. Although substantial progress has been achieved with models and functional continuum methods [1,6–8], input from lattice simulations remains indispensable.

There have been several approaches to circumventing the sign problem, e.g. analytic continuations from imaginary [9–11] or isospin [12,13] chemical potential, which fail, however, when phase transitions are encountered. Another possibility is to combine strong-coupling and hopping expansion techniques to derive an effective theory for heavy quarks [14,15] whose range of applicability must then be assessed. Further alternatives might be provided by stochastic approaches [16], but it is as yet unclear whether they will eventually solve the problem in QCD.

A complementary strategy is to use QCD-like theories without a sign problem. This strategy serves two aims. One is to provide numerical benchmarks for model building [1,6] and continuum methods [7,8], for continuations from imaginary or isospin chemical potential, and equally so for the effective lattice theories for heavy quarks. The other is to gain insight into the genuine properties of gauge theories other than QCD at finite densities, and to exploit analogies with other physical systems such as ultracold fermionic quantum gases. Such QCD-like theories include two-color QCD [17–23] and adjoint QCD [17,24–26]. However, neither of these directly compare well with QCD. Two-color QCD with fundamental quarks does not have fermionic baryons [17,18], while adjoint QCD is known to behave rather differently from QCD already in the quenched case [27].

We have recently added another such replacement theory, G$_2$-QCD [28,29], and shown that it is possible to

---
[*]Bjoern.Wellegehausen@uni-jena.de
[†]axelmaas@web.de
[‡]Wipf@tpi.uni-jena.de
[§]lorenz.smekal@physik.tu-darmstadt.de

simulate this theory at finite density and temperature. This permitted a first view of the full phase diagram of G_2-QCD. We will discuss the properties of this theory in detail in Sec. II. Here, it suffices to state that it can be simulated without the fermion-sign problem at finite density, it does have fermionic baryons, and its properties in the quenched case are very similar to QCD as well. This last observation especially has quite interesting implications for the role of the center symmetry in QCD. A brief review and guide to the literature is given in [30].

In order to better understand the physical picture behind the phase diagram of this theory, however, one needs to understand its hadronic spectrum. In [29] we studied a few low-lying states to give a rough estimate of the scales involved in the simulations. To firmly identify the properties of various finite density phases, we need a much clearer picture of the hadron masses and the corresponding hierarchy of mass scales. These can be deduced from the spectrum of hadronic states in the vacuum. To determine this spectrum from lattice Monte Carlo simulations is the main purpose of the present article. We discuss the theoretical foundations of (lattice) spectroscopy for G_2-QCD in Sec. III. While the lattice determination of the spectrum is in principle straightforward, it is a rather challenging task when it comes to the details, which we describe in Sec. IV. The results for spectra obtained with two different quark masses are presented in Sec. V.

To show that this information is indeed relevant for understanding the phase diagram we relate these results, in an explorative way, to the dependence of the quark density on their chemical potential in Sec. VI. We thereby observe various structures which seem to reflect the hierarchy of scales in the spectrum given by the baryon masses per quark number. Especially, we find an onset at half the would-be-Goldstone mass, a stepwise increase in density at half the intermediate vector boson mass, and a rapid further growth setting in at around one third of the nucleons' mass which is characteristic of their fermionic nature and which might be a manifestation of G_2 nuclear matter. The results indeed suggest that the theory has a rich phase structure, and that baryon-dominated regions of the phase diagram exist before the density is eventually dominated by quarks and lattice artifacts at large chemical potentials. This is of significant importance, as it might indeed point towards the presence of a baryonic Fermi surface, making G_2-QCD a viable model to understand generic features of the finite density phases of the strong interaction.

Our results are summarized once more, together with our conclusions, in Sec. VII. Note that some preliminary material was already presented in [30].

II. GENERAL PROPERTIES OF G_2-QCD

The action of N_f flavor QCD with arbitrary gauge group $\mathcal{G}$ in Minkowski spacetime is given by

$$S = \int d^4x \left\{ -\frac{1}{2} \mathrm{tr} F_{\mu\nu} F^{\mu\nu} \right.$$
$$\left. + \sum_{n=1}^{N_f} \bar{\Psi}_n (i\gamma^\mu(\partial_\mu - gA_\mu) - m)\Psi_n \right\}, \quad (1)$$

with A_μ an element of the corresponding gauge algebra $\mathfrak{g}$. For QCD, the gauge group is $SU(3)$, but here we will use instead the exceptional Lie group G_2. For the sake of completeness, we will briefly review the construction of the gauge group G_2 in Sec. II A, reviewing parts of Ref. [28], before we turn towards the quark sector. The most important ingredient is the Dirac operator, to be discussed in Sec. II B, and the realization of chiral symmetry discussed in Sec. II C. Because G_2 is a real group, chiral symmetry breaking and the concept of baryon number require special attention, as described in Sec. II D.

A. Construction of the gauge group G_2

G_2 is the smallest of the five exceptional simple Lie groups and it is also the smallest simple and simply connected Lie group which has a trivial center. As $SU(3)$, the gauge group of the strong interactions, it has rank 2. The fundamental representations are seven dimensional and 14 dimensional, the latter coinciding with the adjoint representation. The elements of G_2 can be viewed as elements of $SO(7)$ subject to seven independent cubic constraints for the seven-dimensional matrices representing the Lie algebra of $SO(7)$ [28,31],

$$T_{abc} = T_{def} g_{da} g_{eb} g_{fc}, \quad (2)$$

where T is a totally antisymmetric tensor. Its explicit form is basis dependent and examples can be found in [28,31]. There are thus $N_c = 7$ quark colors and 14 gluons in G_2.

The constraints (2) reduce the number of generators from 21 for $SO(7)$ to 14 for the group G_2. In addition, G_2 is connected to $SU(3)$ through the embedding of $SU(3)$ as a subgroup of G_2 according to [32,33],

$$G_2/SU(3) \sim SO(7)/SO(6) \sim S^6. \quad (3)$$

This means that every element $\mathcal{U}$ of G_2 can be written as

$$\mathcal{U} = \mathcal{S} \cdot \mathcal{V} \quad \text{with } \mathcal{S} \in G_2/SU(3) \quad \text{and} \quad \mathcal{V} \in SU(3).$$
$$(4)$$

In the pure G_2 gauge theory [34–36] this decomposition is in fact being used to speed up the numerical simulations. Since G_2 is a subgroup of $SO(7)$, all representations are real and one can always choose a real basis for the Lie algebra. A possible real representation for the 14 generators is given explicitly in Refs. [37,38].

B. The spectrum of the Dirac operator

For lattice Monte Carlo methods to be applicable, the determinant of the Euclidean Dirac operator has to be non-negative. The continuum Dirac operator is given by

$$D[A, m, \mu] = \gamma_{\mathsf{E}}^{\mu}(\partial_{\mu} - gA_{\mu}) - m + \gamma_{\mathsf{E}0}\mu, \qquad (5)$$

where the Euclidean gamma matrices are Hermitian and A is an antisymmetric color matrix. As in QCD the Dirac operator satisfies

$$D(\mu)^{\dagger}\gamma_5 = \gamma_5 D(-\mu^*) \qquad (6)$$

and the fermion determinant is real at imaginary chemical potential. In addition, however, the G$_2$ Dirac operator has an antiunitary symmetry; it also satisfies the relation

$$D(\mu)^* T = T D(\mu^*) \qquad \text{with } T = C\gamma_5,$$
$$T^*T = -\mathbb{1}, \quad T^{\dagger} = T^{-1}, \qquad (7)$$

where C is the charge conjugation matrix. If such a unitary operator T exists then the eigenvalues of the Dirac operator come in complex conjugate pairs and all real eigenvalues are doubly degenerate [17,18], analogous to the Kramers degeneracy of time-reversal invariant spin Hamiltonians. Therefore

$$\det D[A, m, \mu] \geq 0 \quad \text{for } \mu \in \mathbb{R}. \qquad (8)$$

This property of the fermion determinant makes Markov chain Monte Carlo techniques applicable even at finite densities, because the path integral measure $\mathcal{D}A_{\mu} \det D[A, m, \mu] e^{-S_{\mathsf{B}}}$ then essentially provides a probability distribution.

C. Chiral symmetry

In [17], the chiral symmetry of different gauge groups has been investigated. Here we review the details for G$_2$, see also [28]. Under charge conjugation the matter part of the Lagrange density transforms, up to boundary terms, as

$$\mathcal{L}[\Psi^{\mathsf{C}}, A, m] = \mathcal{L}[\Psi, -A^T, m], \qquad (9)$$

with $\Psi = (\Psi_1, …, \Psi_{N_{\mathsf{f}}})$. Therefore, the charge conjugated spinor Ψ^{C} fulfills the same equations of motion as Ψ if the gauge field obeys the condition

$$A_{\mu}^{\mathsf{T}} = -A_{\mu} = -A_{\mu}^a T_a. \qquad (10)$$

Since every representation of G$_2$ is real, the generators T_a of the algebra $\mathfrak{g}_2$ can be chosen as antisymmetric real-valued 7×7 matrices, and hence Eq. (10) holds.

It is then possible to write the matter part of the action (2) as a sum over $2N_{\mathsf{f}}$ Majorana spinors λ_n,

$$\mathcal{L}[\Psi, A] = \bar{\Psi}(\mathrm{i}\gamma^{\mu}(\partial_{\mu} - gA_{\mu}) - m)\Psi$$
$$= \bar{\lambda}(\mathrm{i}\gamma^{\mu}(\partial_{\mu} - gA_{\mu}) - m)\lambda, \qquad (11)$$

with $\lambda = (\chi, \eta) = (\lambda_1, …, \lambda_{2N_{\mathsf{f}}})$. Here λ obeys the Majorana condition $\lambda^{\mathsf{C}} = C\bar{\lambda}^{\mathsf{T}} = \lambda$, $\bar{\lambda}^{\mathsf{C}} = -\lambda^{\mathsf{T}}C^{-1} = \bar{\lambda}$, and it is related to the Dirac spinor as

$$\Psi = \chi + \mathrm{i}\eta, \qquad \bar{\Psi} = \bar{\chi} - \mathrm{i}\bar{\eta},$$
$$\Psi^{\mathsf{C}} = \chi - \mathrm{i}\eta, \qquad \bar{\Psi}^{\mathsf{C}} = \bar{\chi} + \mathrm{i}\bar{\eta}. \qquad (12)$$

Therefore, it follows that G$_2$-QCD possesses an extended flavor symmetry as compared to $SU(3)$-QCD.

The action is invariant under the $SO(2N_{\mathsf{f}})_{\mathsf{V}}$ vector transformations

$$\lambda \mapsto e^{\beta \otimes \mathbb{1}}\lambda \qquad (13)$$

with a real and antisymmetric $\beta \in \mathfrak{so}(2N_{\mathsf{f}})$, and under the axial transformations

$$\lambda \mapsto e^{\mathrm{i}\alpha \otimes \gamma_5}\lambda \qquad (14)$$

with a real symmetric matrix α. These do not form a group, but the transformations with diagonal α form the group $U(1)^{2N_{\mathsf{f}}}$ and those with $\alpha \propto \mathbb{1}$ among them generate the axial $U(1)$. Due to the Majorana constraint left- and right-handed spinors cannot be rotated independently. The general transformation is a composition of an axial and a vector transformation,

$$\lambda \mapsto e^{\beta \otimes \mathbb{1}} e^{\mathrm{i}\alpha \otimes \gamma_5}\lambda \equiv V(\alpha, \beta)\gamma$$
$$V = \mathrm{U}(\alpha, \beta) \otimes \mathsf{P}_{\mathsf{L}} + \mathrm{U}^*(\alpha, \beta) \otimes \mathsf{P}_{\mathsf{R}}, \qquad (15)$$

with an $U(2N_{\mathsf{f}})$-matrix $U(\alpha, \beta) = e^{\beta} e^{\mathrm{i}\alpha}$, in agreement with the results in [28]. Following the same arguments as in QCD it is expected that the axial $U(1)$ is broken by the axial anomaly such that only an extended $SU(2N_{\mathsf{f}}) \times \mathbb{Z}(2)_{\mathsf{B}}$ chiral symmetry remains.

D. Chiral symmetry breaking and baryon number

In the presence of a nonvanishing Dirac mass term (or a nonvanishing chiral condensate) the theory is no longer invariant under the axial transformations. Therefore the nonanomalous chiral symmetry is expected to be broken explicitly (or spontaneously) to its maximal vector subgroup,

$$SU(2N_{\mathsf{f}}) \otimes \mathbb{Z}(2)_{\mathsf{B}} \overset{m}{\mapsto} SO(2N_{\mathsf{f}})_{\mathsf{V}} \otimes \mathbb{Z}(2)_{\mathsf{B}}, \qquad (16)$$

leading to $N_{\mathsf{f}}(2N_{\mathsf{f}} + 1) - 1$ (would-be) Goldstone bosons.

The (baryon) chemical potential for a Dirac fermion enters the partition function as an off-diagonal term in Majorana flavor space,

$$\mathcal{L} = \bar{\Psi}(iD - m + i\gamma_0\mu)\Psi$$

$$= \begin{pmatrix} \bar{\chi} \\ \bar{\eta} \end{pmatrix} \begin{pmatrix} iD - m & i\gamma_0\mu \\ -i\gamma_0\mu & iD - m \end{pmatrix} \begin{pmatrix} \chi \\ \eta \end{pmatrix}. \qquad (17)$$

With chemical potential but vanishing Dirac mass the remaining chiral symmetry is thus the same as in QCD,

$$SU(2N_f) \otimes \mathbb{Z}(2)_B \overset{\mu}{\mapsto}$$
$$SU(N_f)_A \otimes SU(N_f)_V \otimes U(1)_B/\mathbb{Z}(N_f). \qquad (18)$$

For $m \neq 0$ the remaining chiral symmetry is further broken as

$$SU(N_f)_A \otimes SU(N_f)_V \otimes U(1)_B/\mathbb{Z}(N_f) \overset{\mu,m}{\mapsto}$$
$$SU(N_f)_V \otimes U(1)_B/\mathbb{Z}(N_f). \qquad (19)$$

If one first introduces a mass and only afterwards a chemical potential, then one notices that for $\mu \neq 0$ the Lagrangian is off diagonal in the Majorana basis such that is not possible to transform the Majorana components of a Dirac spinor independently. Therefore, the vector symmetry $SO(2N_f)_V$ of the massive theory is further reduced to transformations that do not interchange the Majorana spinors. However, complex transformations are allowed, leading to the residual $SU(N_f)_V$ symmetry group.

The pattern of chiral symmetry breaking in G_2-QCD is summarized in Fig. 1. If chiral symmetry is spontaneously broken, the axial chiral multiplet becomes massless according to Goldstone's theorem. In contrast to QCD, because of the extended chiral symmetry group, in the case of a single Dirac flavor it already contains a nontrivial $SU(2)$ and chiral symmetry breaking is possible. This is one reason why in the following only G_2-QCD with a single Dirac flavor $N_f = 1$ is investigated. The chiral symmetry is then given by

$$SU(2) \otimes \mathbb{Z}(2)_B. \qquad (20)$$

The corresponding creation operators for the Goldstone bosons are given by

$$d(0^{++}) = \bar{\chi}\gamma_5\eta = \frac{1}{4i}(\bar{\Psi}^C\gamma_5\Psi - \bar{\Psi}\gamma_5\Psi^C),$$

$$d(0^{+-}) = \frac{1}{\sqrt{2}}(\bar{\chi}\gamma_5\chi - \bar{\eta}\gamma_5\eta) = \frac{1}{2\sqrt{2}}(\bar{\Psi}^C\gamma_5\Psi + \bar{\Psi}\gamma_5\Psi^C). \qquad (21)$$

As usual, the baryon number n_B is here defined as the transformation behavior of an operator under the $U(1)$ subgroup of the vector chiral transformation,

$$\Psi \mapsto e^{in_B\alpha}\Psi, \qquad (22)$$

such that a quark has the baryon number $n_B = 1$ and an antiquark $n_B = -1$. With this definition of the baryon number the Goldstone bosons have $n_B = 2$. In the single flavor theory the scalar diquarks are the only Goldstone bosons. The pseudoscalar mesons become part of the larger Goldstone boson multiplet with the extended chiral $SU(2N_f)$ symmetry for $N_f \geq 2$.

III. SPECTROSCOPY FOR $N_f = 1$ G_2-QCD

The possible quark and gluon content of (colorless) bound states is determined by the tensor products of G_2-QCD. Quarks in G_2 transform under the seven-dimensional fundamental representation, gluons under the 14-dimensional fundamental (and at the same time adjoint) representation. The decomposition of tensor products of the lowest-dimensional representations into irreducible representations is given by

$$(7) \otimes (7) = (1) \oplus (7) \oplus (14) \oplus (27),$$
$$(7) \otimes (7) \otimes (7) = (1) \oplus 4 \cdot (7) \oplus 2 \cdot (14) \oplus 3 \cdot (27)$$
$$\oplus 2 \cdot (64) \oplus (77'),$$
$$(14) \otimes (14) = (1) \oplus (14) \oplus (27) \oplus (77) \oplus (77'),$$
$$(14) \otimes (14) \otimes (14) = (1) \oplus (7) \oplus 5 \cdot (14)$$
$$\oplus 3 \cdot (27) \oplus \cdots,$$
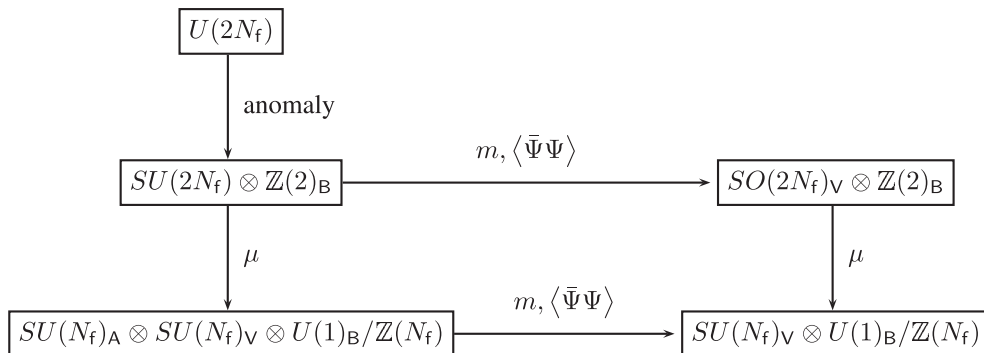$$(7) \otimes (14) \otimes (14) \otimes (14) = (1) \oplus \cdots. \qquad (23)$$

FIG. 1. Pattern of chiral symmetry breaking in G_2-QCD.

Thus we expect to find bound states for every integer quark number n_q. Mesons have $n_q = 0$, diquarks $n_q = 2$, and nucleons $n_q = 3$. In addition, there are more exotic bound states of gluons and quarks, for example a hybrid with $n_q = 1$. The latter state would be especially important, as the nucleons will only be stable in the chiral limit if the hybrid is heavier than the nucleon. Of course, more complicated states with higher baryon numbers are possible, as well as glueballs, but are expected to play no role either in the vacuum or at the moderate densities we investigate here.

In the following we give an overview of our implementation of possible bound states for $N_f = 2$, see Tables I–IV. The subset of states of the one-flavor model, treated numerically below, are easily recognized.

In all tables $\mathcal{O}$ is the interpolating operator used to extract the mass in simulations, T the behavior of the wave function under change of position, spin, color and flavor (S stands for symmetric, A for antisymmetric), and the spin (J), parity (P) and charge conjugation (C) quantum

TABLE I. Bound states of G$_2$-QCD with two flavors and baryon number $n_B = 0$. For details see text.

Name	$\mathcal{O}$	T	J	P	C
π	$\bar{u}\gamma_5 d$	SASS	0	$-$	$+$
η	$\bar{u}\gamma_5 u$	SASS	0	$-$	$+$
a	$\bar{u}d$	SASS	0	$+$	$+$
f	$\bar{u}u$	SASS	0	$+$	$+$
ρ	$\bar{u}\gamma_\mu d$	SSSA	1	$-$	$+$
ω	$\bar{u}\gamma_\mu u$	SSSA	1	$-$	$+$
b	$\bar{u}\gamma_5\gamma_\mu d$	SSSA	1	$+$	$+$
h	$\bar{u}\gamma_5\gamma_\mu u$	SSSA	1	$+$	$+$

TABLE II. Bound states with baryon number $n_B = 1$. For details see text.

Name	$\mathcal{O}$	T	J	P	C
N'	$T^{abc}(\bar{u}_a\gamma_5 d_b)u_c$	SAAA	1/2	$\pm$	$\pm$
Δ'	$T^{abc}(\bar{u}_a\gamma_\mu u_b)u_c$	SSAS	3/2	$\pm$	$\pm$
Hybrid	$\epsilon_{abcdefg}u^a F^{bc}_{\mu\nu}F^{de}_{\mu\nu}F^{fg}_{\mu\nu}$	SSSS	1/2	$\pm$	$\pm$

TABLE III. Bound states with baryon number $n_B = 2$. For details see text.

Name	$\mathcal{O}$	T	J	P	C
$d(0^{++})$	$\bar{u}^C\gamma_5 u +$ c.c.	SASS	0	$+$	$+$
$d(0^{+-})$	$\bar{u}^C\gamma_5 u -$ c.c.	SASS	0	$+$	$-$
$d(0^{-+})$	$\bar{u}^C u +$ c.c.	SASS	0	$-$	$+$
$d(0^{--})$	$\bar{u}^C u -$ c.c.	SASS	0	$-$	$-$
$d(1^{++})$	$\bar{u}^C\gamma_\mu d - \bar{d}^C\gamma_\mu u +$ c.c.	SSSA	1	$+$	$+$
$d(1^{+-})$	$\bar{u}^C\gamma_\mu d - \bar{d}^C\gamma_\mu u -$ c.c.	SSSA	1	$+$	$-$
$d(1^{-+})$	$\bar{u}^C\gamma_5\gamma_\mu d - \bar{d}^C\gamma_5\gamma_\mu u +$ c.c.	SSSA	1	$-$	$+$
$d(1^{--})$	$\bar{u}^C\gamma_5\gamma_\mu d - \bar{d}^C\gamma_5\gamma_\mu u -$ c.c.	SSSA	1	$-$	$-$

TABLE IV. Bound states with baryon number $n_B = 3$. For details see text.

Name	$\mathcal{O}$	T	J	P	C
N	$T^{abc}(\bar{u}_a^C\gamma_5 d_b)u_c$	SAAA	1/2	$\pm$	$\pm$
Δ	$T^{abc}(\bar{u}_a^C\gamma_\mu u_b)u_c$	SSAS	3/2	$\pm$	$\pm$

numbers. States with baryon number 0 and 3 are also present in QCD, while the others are additional states of G$_2$-QCD.

In our simulations the states of the two-flavor model are included by partial quenching; that means we are dealing with two valence quark flavors, but only one sea quark flavor. In QCD, this is a surprisingly good approximation, see e. g. [39], and there is no obvious reason why this should be different in G$_2$-QCD.

There is one particular caveat, which is due to the limitation in computational resources for this project. The diquark correlation function that we measure on the lattice is given by

$$C_d(x,y) = \langle d(0^{++})(x)\, d(0^{++})^\dagger(y)\rangle$$
$$= \langle d(0^{+-})(x)\, d(0^{+-})^\dagger(y)\rangle$$
$$= \left\langle \bar{\chi}(x)\gamma_5\chi(x)\,\bar{\chi}(y)\gamma_5,\chi(y)\right\rangle \quad (24)$$

showing that the diquark masses are degenerate and its correlation functions contain only connected contributions, like for example the correlation function for the pion in QCD. The corresponding correlation function for the η meson reads

$$C_\eta(x,y) = \langle\eta(x)\,\eta^\dagger(y)\rangle$$
$$= 2\left\langle \bar{\chi}(x)\gamma_5\chi(x)\,\bar{\chi}(y)\gamma_5\chi(y)\right\rangle + C_d(x,y) \quad (25)$$

The difference between the η and the diquark correlation function is only the disconnected contribution. Therefore, uncertainties in the treatment of the disconnected contribution can blur the line between the η and the diquarks.

Analog relations lead for the partially quenched calculations performed here to some relations between flavor singlet diquark masses and flavor nonsinglet meson masses,

$$m_{d(0^+)} = m_{\pi(0^-)}$$
$$m_{d(0^-)} = m_{a(0^+)}$$
$$m_{d(1^+)} = m_{\rho(1^-)}$$
$$m_{d(1^-)} = m_{b(1^+)}. \quad (26)$$

Thus, for every diquark there is a flavor nonsinglet meson with the same mass but opposite parity.

IV. ALGORITHMIC CONSIDERATIONS

In our lattice simulations we use a hybrid Monte Carlo algorithm [40] to generate the probability distribution. Our implementation is based on [35], where the algorithm was applied to G_2-Yang-Mills-Higgs theory.

For the gauge action we choose the tree-level improved Symanzik gauge action [41–44]

$$S[\mathcal{U}] = \frac{\beta}{N_c}\left\{c_0\sum_{\square}\text{tr}(1-\text{Re}\mathcal{U}_{\square})+c_1\sum_{\square\square}\text{tr}(1-\text{Re}\mathcal{U}_{\square\square})\right\}. \tag{27}$$

Here, $\mathcal{U}_{\square}$ stands for the plaquette variable and $\mathcal{U}_{\square\square}$ for a rectangular path around two plaquettes. The parameters are given by $c_0 = 1 - 8c_1$, $c_1 = -1/2$. Note that our convention is to factorize the number of colors from β.

For the fermion part, we use the ordinary Wilson action without improvements [3]. Though we cannot expect good chiral properties in this case, we can avoid rooting for staggered fermion. Using unrooted staggered fermions, and thus four flavors, would on the one hand create far too many Goldstone bosons, and would possibly put the theory too close or in the conformal window, according to the two-loop β-function. Fermion implementations with better chiral properties are unfortunately beyond our numerical resources.

For the fermion determinant we use pseudofermions together with a rational approximation of the inverse fermion matrix (RHMC algorithm) [45]. In the case of Dirac fermions the path integral is given by[1]

$$\mathcal{Z} = \int \mathcal{D}\Psi\mathcal{D}\bar{\Psi}\mathcal{D}\mathcal{U}e^{-S[\mathcal{U}]-\text{tr}\bar{\Psi}D\Psi}$$

$$= \mathcal{N}\int \mathcal{D}\mathcal{U}\det(D[\mathcal{U}])e^{-S[\mathcal{U}]}$$

$$= \mathcal{N}\int \mathcal{D}\mathcal{U}\det(M[\mathcal{U}]^{\frac{1}{2}})e^{-S[\mathcal{U}]}, \tag{28}$$

where D is the fermion operator and $M = D^\dagger D$ is a Hermitian and positive operator. Introducing N_{PF} complex-valued pseudo-fermions ϕ [46], one can write the partition function as

$$\mathcal{Z} = \int \mathcal{D}\mathcal{U}\mathcal{D}\phi\exp\{-S_B[\mathcal{U},\phi]\}$$

$$\text{with } S_B[\mathcal{U},\phi] = S[\mathcal{U}] + \text{tr}\sum_{p=1}^{N_{\text{PF}}}\phi_p^\dagger M^{-q}\phi_p, \tag{29}$$

where S_B is the bosonic action and q is given by $q = \frac{1}{2N_{\text{PF}}}$. In the RHMC dynamics M^{-q} is replaced by a rational approximation according to

$$r(x) = x^{-q} \approx \alpha_0 + \sum_{r=1}^{N_R}\frac{\alpha_r}{x+\beta_r}. \tag{30}$$

For any rational number q the coefficients α and β can be calculated with the Remez algorithm [47]. The numerical accuracy of the approximation in the interval $I = [x_{\text{Min}}, x_{\text{Max}}]$ depends on the number of terms N_R in (30) and the numerical accuracy of the coefficients α and β. In the following $r_S(x), S = \{I, \epsilon, q\}$ denotes a rational approximation of the function x^{-q} with $\epsilon = \sup_{x\in I}||r(x) - x^{-q}||$.

In order to obtain an exact update algorithm, the bosonic action is written in the form

$$S_B[\mathcal{U},\phi] = S[\mathcal{U}] + S_{\text{md}}(M) + S_{\text{acc}}(M) + S_{\text{rw}}(M), \tag{31}$$

where the different contributions are given by

$$S_{\text{md}} = \text{tr}\sum_{p=1}^{N_{\text{PF}}}\phi_p^\dagger r_{S_{\text{md}}}\phi_p,$$

$$S_{\text{acc}} = \text{tr}\sum_{p=1}^{N_{\text{PF}}}\phi_p^\dagger(r_{S_{\text{acc}}}(M) - r_{S_{\text{md}}}(M))\phi_p,$$

$$S_{\text{rw}} = \text{tr}\sum_{p=1}^{N_{\text{PF}}}\phi_p^\dagger(M^{-q} - r_{S_{\text{acc}}}(M))\phi_p. \tag{32}$$

The sum $S[\mathcal{U}] + S_{\text{md}}(M)$ is used in the calculation of the HMC molecular dynamics, the sum $S[\mathcal{U}] + S_{\text{md}}(M) + S_{\text{acc}}(M)$ in the Metropolis acceptance step of the HMC algorithm and the last term $S_{\text{rw}}(M)$ in a reweighting step to ensure an exact update algorithm.

In practice, the reweighting step is not necessary since it is more efficient to choose $r_{S_{\text{acc}}}$ such that it approximates M^{-q} up to machine precision. For the generation of the pseudofermion fields from a Gaussian distributed vector the square root of M^q is needed as well. This is achieved by an approximation $r_{S_{\text{pf}}}(M) \approx M^{q/2}$. To obtain an exact update algorithm, the following choices are made:

$$r_{S_{\text{pf}}}(M) = \{I \supseteq \Sigma(M), 10^{-16}, -q/2\},$$

$$r_{S_{\text{acc}}}(M) = \{I \supseteq \Sigma(M), 10^{-16}, q\}, \tag{33}$$

where $\Sigma(M) = [\lambda_{\text{min}}, \lambda_{\text{max}}]$ is the spectral range of the Hermitian operator M. In most of the simulations, an approximation for the pseudofermion and acceptance step approximation of degree $N_R = 25$ is used in an interval $I = [10^{-7}, 10]$.

The free parameters left to optimize the algorithm are the integration scheme used in the molecular dynamics and the degree and approximation range of the molecular dynamics rational approximation $r_{S_{\text{md}}}(M)$. The inversions of the matrix M in the rational approximations are calculated with a multiple-mass conjugate gradient solver

---

[1]Below, tr denotes the integral over d-dimensional spacetime and the trace over all internal degrees of freedom.

(MMCG) [48] which is able to compute all terms of (30) within a single inversion of the fermion matrix M.

A. Symplectic integration and multiple time scales

In order to speed up our simulation, we use integration on different time scales in a HMC trajectory. The simplest possible integration scheme is the leapfrog scheme [49]. The time evolution T from $\tau = 0$ to $\tau = t_{\mathsf{HMC}}$ with step size $\delta\tau = \frac{t_{\mathsf{HMC}}}{n}$ with the leapfrog time evolution operator T_{LF} can be written as

$$T(t_{\mathsf{HMC}}, \delta\tau) = T_{\mathsf{LF}}(\delta\tau)^n,$$

$$T_{\mathsf{LF}}(\delta\tau) = T_S\left(\frac{1}{2}\delta\tau\right)T_{\mathcal{U}}(\delta\tau)T_S\left(\frac{1}{2}\delta\tau\right), \quad (34)$$

where T_S describes time evolution for the momenta and $T_{\mathcal{U}}$ for the fields. An improved second-order integrator is given by the Sexton-Weingarten scheme [50],

$$T_{\mathsf{SW}}(\delta\tau) = T_S\left(\frac{\delta\tau}{6}\right)T_{\mathcal{U}}\left(\frac{\delta\tau}{2}\right)T_S\left(\frac{2\delta\tau}{3}\right)T_{\mathcal{U}}\left(\frac{\delta\tau}{2}\right)T_S\left(\frac{\delta\tau}{6}\right).$$

$$(35)$$

A fourth-order integrator is given by [51],

$$T_4(\delta\tau) = T_S(\rho\delta\tau)T_{\mathcal{U}}(\lambda\delta\tau)T_S(\theta\delta\tau)$$

$$\times T_{\mathcal{U}}\left((1-2\lambda)\frac{\delta\tau}{2}\right)T_S((1-2(\theta+\rho))\delta\tau)$$

$$\times T_{\mathcal{U}}\left((1-2\lambda)\frac{\delta\tau}{2}\right)T_S(\theta\delta\tau) \times T_{\mathcal{U}}(\lambda\delta\tau)T_S(\rho\delta\tau),$$

$$(36)$$

with parameter values

$$\rho = 0.1786178958448091,$$

$$\theta = 0.06626458266981843 \quad \text{and}$$

$$\lambda = 0.7123418310626056. \quad (37)$$

Higher-order integrators are constructed in [52]. Further improvement can be achieved by integration on multiple time scales [53]. For this purpose an arbitrary integrator T_{s} (here s stands for the integration scheme) is written as a function of the basic time evolution operators T_S and $T_{\mathcal{U}}$ and the integration step size $\delta\tau$, $T_{\mathsf{s}} = T_{\mathsf{s}}(T_S, T_{\mathcal{U}}, \delta\tau)$.

If the action can be written as a sum of contributions S_j, i.e. $S = S_1 + S_2 + \ldots$, then multiple time scale integration can be defined by the recursion relation

$$T_{\mathsf{s}_j}^j(T_{S_j}, T_{\mathcal{U}}, \delta\tau_j) = T_{\mathsf{s}_j}^j(T_{S_j}, [T_{\mathsf{s}_{j-1}}^{j-1}(T_{S_{j-1}}, T_{\mathcal{U}}, \delta\tau_j/n_j)]^{n_j}, \delta\tau_j),$$

$$(38)$$

where S_j denotes the subset of the action that should be taken into account in the computation of the "force" on the jth time scale with step size $\delta\tau_j$. Here, we often use a two-time-scale integration, which is a combination of the Sexton-Weingarten scheme with the leapfrog scheme,

$$T(\delta\tau) = T_{S_0}\left(\frac{\delta\tau}{2}\right)T_{\mathsf{SW}}(T_{S_1}, T_{\mathcal{U}}, \delta\tau)T_{S_0}\left(\frac{\delta\tau}{2}\right)$$

$$= T_{S_0}\left(\frac{\delta\tau}{2}\right)T_{S_1}\left(\frac{\delta\tau}{6}\right)T_{\mathcal{U}}\left(\frac{\delta\tau}{2}\right)$$

$$\times T_{S_1}\left(\frac{2\delta\tau}{3}\right)T_{\mathcal{U}}\left(\frac{\delta\tau}{2}\right)T_{S_1}\left(\frac{\delta\tau}{6}\right)T_{S_0}\left(\frac{\delta\tau}{2}\right). \quad (39)$$

Here, the force according to S_1 has to be calculated twice as often as the force belonging to S_0.

Another scheme often used is the combination of a fourth-order integrator with the Sexton-Weingarten scheme or with the simple leapfrog scheme. Multiple-time-scale integration is efficient if parts of the action with large contribution to the HMC force are cheap in computation time.

B. Optimization of the RHMC algorithm

The efficiency of the RHMC algorithm depends crucially on the lowest eigenvalues entering the condition number $\kappa \approx \lambda_{\max}/\lambda_{\min}$ of the Hermitian operator used in the rational approximation. The number of total inversion steps for a given precision $\delta_{\max}$ (the inversion precision for the lowest mass, i.e. the lowest value of β_r) in the MMCG solver increases significantly with decreasing values of the constants β_r in the rational approximation. Fortunately, the force contribution in the RHMC algorithm is for small constants also significantly lower than for larger constants (the reason is that α_r decreases also with decreasing β_r). The force from these lowest eigenmodes becomes more important only in the case of very small eigenvalues.

This feature of the RHMC algorithm can now be used to optimize the algorithm with respect to computation time. Two different strategies are useful: The first is to integrate the terms with smaller β_r on a coarser time scale than the terms with larger β_r, i.e. larger force. The second is to increase the lower bound of the approximation interval, resulting in larger values of β_r and a possibly smaller degree of the rational function used for the molecular dynamics. This reduces the number of CG steps for a given inversion precision $\delta_{\max}$ significantly.

Further optimization can be achieved by increasing the precision $\delta_{\max}$ used for the inversion, also leading to a significantly reduced number of CG steps. The best choice of course depends on the given problem and is in general a combination of both strategies. Further optimizations implemented include even-odd preconditioning [54] as well as an exact computation of a few lowest eigenvalues in the MMCG solver. According to [55], the optimal

number of pseudofermions is roughly given by the condition number of the fermion matrix, $N_{PF}^{opt} \approx \frac{1}{n} \ln \kappa(M)$.

C. Fermionic correlation functions

For the computation of the connected part of the correlation function, the fermion matrix is inverted on a pointlike source in space and time at a randomly chosen lattice point y, leading to the point-to-all propagator. Here, $N_c \times N_s$ (number of colors times the dimension of the representation of the Clifford algebra) inversions of the fermion matrix with the CG solver have to be made.

The disconnected diagrams, and for instance observables like the chiral condensate or the quark number density, are calculated with the stochastic estimator technique [56,57]. Here every element of the fermion propagator is calculated as an ensemble average over a noisy estimator η,

$$\tilde{\Delta}_{ij} = \lim_{N_{est} \to \infty} \langle \eta_j^\dagger \chi_i \rangle \qquad \text{with}$$

$$\chi = \tilde{\Delta} \eta \quad \text{and} \quad \lim_{N_{est} \to \infty} \langle \eta_i^\dagger \eta_j \rangle = \delta_{ij}. \qquad (40)$$

In practice, the ensemble average is taken over a finite number of N_{est} noisy estimators, where the source η is given by Gaussian or $\mathbb{Z}(2)$ noise, satisfying the last equation in (40). The sink is again calculated with a CG solver, making a total of N_{est} matrix inversions to obtain an estimator for every matrix element of the propagator. In the case of local lattice averaged observables, like the chiral condensate, a number of $N_{est} \approx 10$ estimators is sufficient to get a reliable result. For the disconnected part of four-point correlation functions (many) more estimators are necessary.

Note that we extract the masses from the correlators $C(t)$ by fits of the type

$$C(t) = a \cosh(mt) + b \cosh(m^*t), \qquad (41)$$

or with a single-cosh fit, where a double-cosh fit was not possible. The quoted errors denote only the statistical error from a simultaneous up- or down-shift of the correlation function by one standard deviation.

We identify the smaller of the two parameters m and m^* in (41) as the ground state mass, and mark the next higher mass with an asterisk '*'. We do not make any attempt to identify whether these are genuine excited states or merely scattering states, and, as noted in Sec. III, we use a single operator per quantum number channel. We also do not attempt to identify whether the lowest state is a genuine bound state or a scattering state, even if it appears energetically favorable for them to decay. For some states we are also limited by statistics, and thus could not measure the mass of all relevant channels. This applies especially to the hybrids. We therefore have to assume in the following that at least the ground states are reasonably stable states.

V. LATTICE SPECTROSCOPY RESULTS

In order to fix our parameters we compute the diquark masses and the proton mass for different parameters of the inverse gauge coupling β and the hopping parameter κ on a $8^3 \times 16$ lattice. We make here the implicit assumption that the nucleon is (quasi) stable, i.e. it is not energetically favorable or possible for it to decay into a hybrid and a diquark. Since the hybrids were too noisy to obtain reliable results, we could not check this assumption.

To assess the distance from the chiral limit, we first compare the Goldstone sector to the nucleon sector. In Fig. 2 the $d(0^+)$ mass is shown as a function of the inverse gauge coupling β for a fixed value of the hopping parameter κ. In Fig. 3 the proton mass is plotted for the same parameters.

Care has to be taken, as G_2-QCD possesses an unphysical lattice bulk phase at strong coupling where monopoles condense. The critical inverse gauge coupling for the
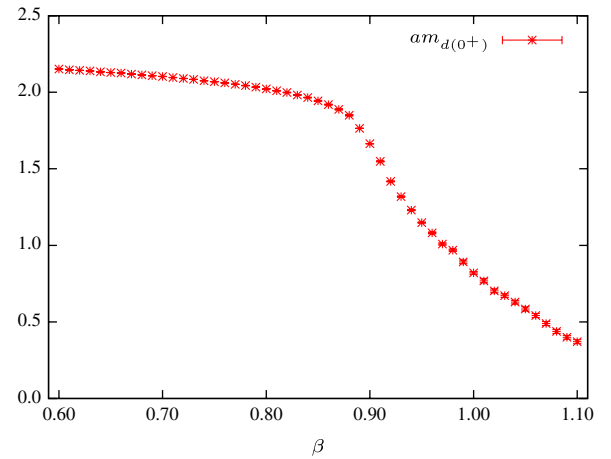
FIG. 2 (color online).   Mass of the pseudo-Goldstone boson as a function of β for $\kappa = 0.147$.
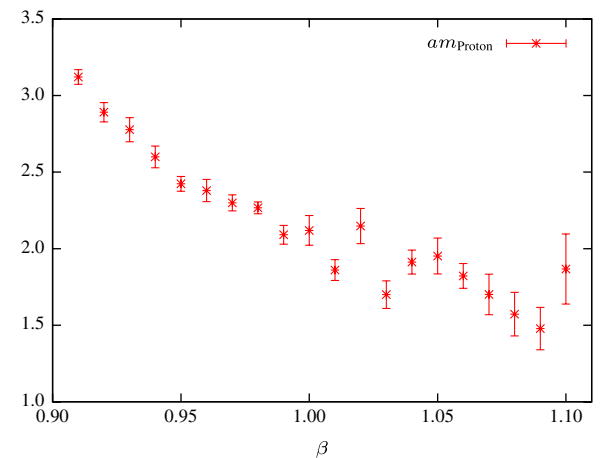
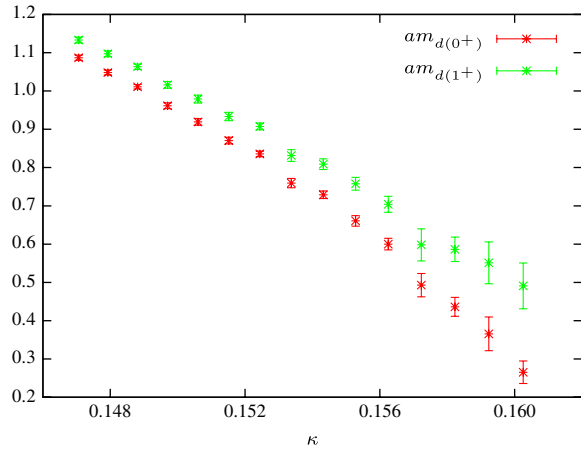FIG. 3 (color online).   Mass of the proton as a function of β for $\kappa = 0.147$.

FIG. 4 (color online). Mass of the 0^+ and the 1^+ diquark as a function of κ for $\beta = 0.96$.

FIG. 5 (color online). Mass spectrum of the heavy ensemble.

FIG. 6 (color online). Mass spectrum of the light ensemble.

transition to the physical weak coupling phase depends on the hopping parameter. For $\kappa = 0.147$ it is located around $\beta \approx 0.90$. We observe that in the bulk phase the lattice diquark mass depends only rather weakly on the gauge coupling which is unphysical. Above the transition, the diquark mass in lattice units decreases with increasing β as it must in order to define a proper continuum limit. Since the bulk transition is a crossover (at least for infinitely heavy quarks [34,58]) we have to choose a gauge coupling for our simulations that is far above the transition point. For our spectroscopy results we have checked that the monopole density is always below 1 percent of the monopole saturation density in the bulk phase.

For heavy quarks the ratio of diquark and proton mass should be 2/3 while it should go to zero in the chiral limit. A second mass ratio to fix the bare parameters is the ratio of the 0^+ and the 1^+ diquark. For heavy quarks only the number of quarks is important and the ratio should be 1, while in the chiral limit the spin zero diquark becomes massless while the spin one diquarks stay massive. The results for the masses are shown in Fig. 4 as a function of κ and fixed β. Indeed we see that for smaller Goldstone masses the ratio increases. In the following we discuss two different ensembles with parameters shown in Table V. In the following, we will set our mass scale by the proton mass, $m_N = 938$ MeV.

The mass spectrum for the heavy quark ensemble is shown in Fig. 5. The diquark masses are almost degenerate. Also the η has essentially the same mass as the diquarks. For the nucleons there is almost no mass splitting between parity even and odd states.
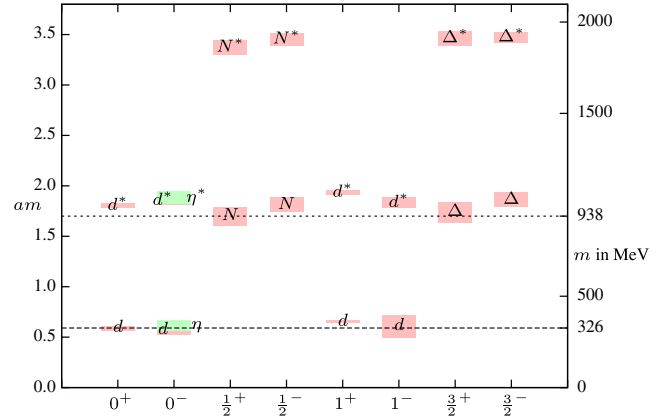
In the light ensemble, shown in Fig. 6, the diquark masses are no longer degenerate. We observe a significant mass splitting between parity even and odd states as well as between scalar and vector diquarks. In particular, the Goldstone boson becomes the lightest state, with the η also being somewhat heavier. This mass difference comes entirely from the disconnected part of the meson correlation function in (25). For the nucleons we also observe different masses for parity even and odd states and the spin 1/2 and spin 3/2 representations. Thus, the spectrum is indeed consistent with spontaneous chiral symmetry breaking, in accordance with quenched [27] and previous results [29]. In particular, we find three clearly different scales in the light spectrum: a Goldstone scale, an intermediate boson scale set by the remaining diquarks, and the nucleon scale set by the N and Δ.

TABLE V. Parameters for two different ensembles. All results are from a $8^3 \times 16$ lattice.

Ensemble	β	κ	$m_{d(0^+)}a$	$m_N a$	$m_{d(0^+)}$ [MeV]	a [fm]	a^{-1} [MeV]	MC
Heavy	1.05	0.147	0.59(2)	1.70(9)	326	0.357(33)	552(50)	7 K
Light	0.96	0.159	0.43(2)	1.63(13)	247	0.343(45)	575(75)	5 K

VI. G$_2$-QCD AT ZERO TEMPERATURE AND FINITE BARYON DENSITY

A. Overview

In [29] we provided an overview over the full phase diagram of G$_2$-QCD as a function of temperature and baryon density. We will now show that the different hadronic scales observed in the spectra in Figs. 5 and 6 reflect themselves in the structure of the finite density phase diagram.

The first scale, the Goldstone scale, must be related to the onset transition to baryonic matter, since the Goldstones carry a quark number. This follows immediately from the silver blaze property of quantum field theories [59] at zero temperature and finite density.

To investigate this regime, we have calculated the quark number density n_q given by

$$n_q = \frac{1}{V} \frac{\partial \ln Z}{\partial \mu}. \tag{42}$$

In [29] we observed that for small values of the chemical potential the system remains in the vacuum, i.e. the quark number density vanishes, which is expected due to the silver blaze property. When increasing the chemical potential further the quark number density starts rising, indicating that baryonic matter is present and the system is no longer in the vacuum state. At even larger values of μ the quark number density saturates. The value of the saturation matches the theoretical prediction of $n_{q,\max} = 2N_c = 14$ [29]. This is depicted in Fig. 7.

The same figure shows the dependence of the Polyakov loop on the chemical potential from $\mu = 0$ up to saturation. The decrease of the Polyakov loop close to saturation also indicates that the system enters a quasiquenched phase, where the quark dynamics freezes out [19,29]. This
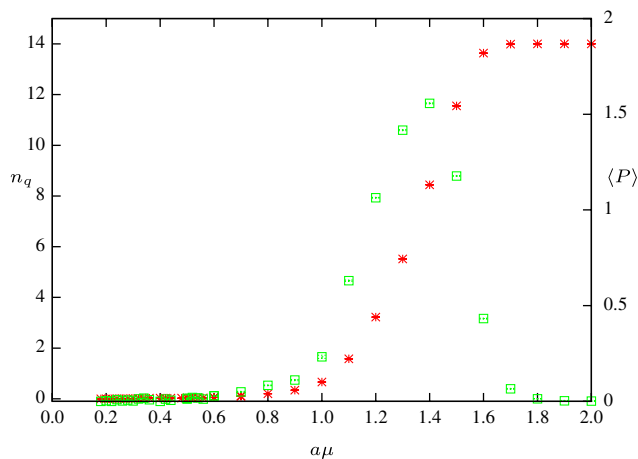

FIG. 7 (color online). Quark number density in lattice units (red stars) and Polyakov loop (green squares) as a function of chemical potential. Saturation occurs when the finite lattice starts to get filled with the maximum number of fermions, which leads to an artificial behavior above $a\mu \approx 1$.
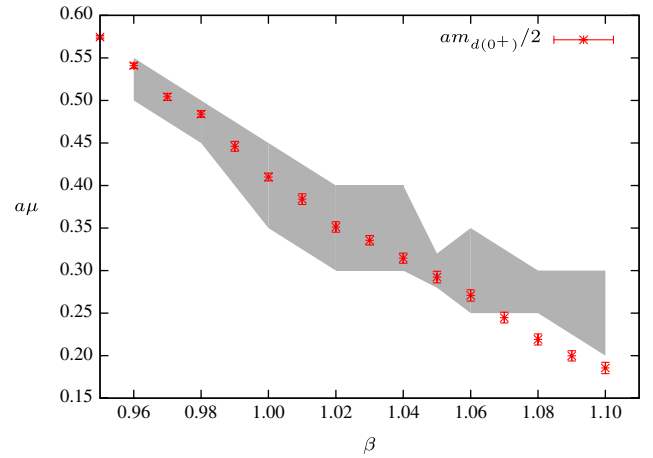

FIG. 8 (color online). The onset transition observed in the quark number density is compared to half of the mass of the lightest state, the 0^+ diquark, for different gauge couplings β, and thus different quark masses.

emphasizes that for $a\mu \approx 1$ lattice artifacts start to dominate the system. However, this is for both ensembles at an already high quark chemical potential of about 550 MeV, corresponding to a nucleon chemical potential of 1.65 GeV. Therefore we focus on the region $a\mu \leq 1$ from now on.

B. Scales at finite density

A closer look into this phase diagram at zero temperature shows that the quark number density jumps, or very quickly rises, to a very small, but nonzero, value already at a very small chemical potential. In Fig. 8 this onset transition is compared to half of the mass of the lightest baryon, the Goldstone 0^+ diquark. For various values of β very good agreement is found. This is the expected manifestation of the silver blaze property for baryon chemical potential, i.e. half of the mass of the lightest bound state carrying a baryon number is a lower bound for the onset transition to a nonvacuum state.[2]

For larger values of the chemical potential a series of plateaus develop where the quark number density is almost constant, see Fig. 9 for the heavy ensemble and Fig. 10 for the light ensemble. In both cases, we observe at intermediate chemical potential interesting structures, which will be discussed below. At around $a\mu = 0.6$ for the heavy ensemble and $a\mu = 0.55$ for the light ensemble the quark number density starts increasing again and no further plateau is observed.

---

[2]Note that a finite lattice is strictly speaking never at zero temperature, and therefore the silver blaze property is never exactly realized. The finiteness of the spatial volume has analogous effects. Although they are exponentially suppressed in general, regions close to a phase transition are very sensitive to those finite-size effects. We do indeed observe such artifacts.
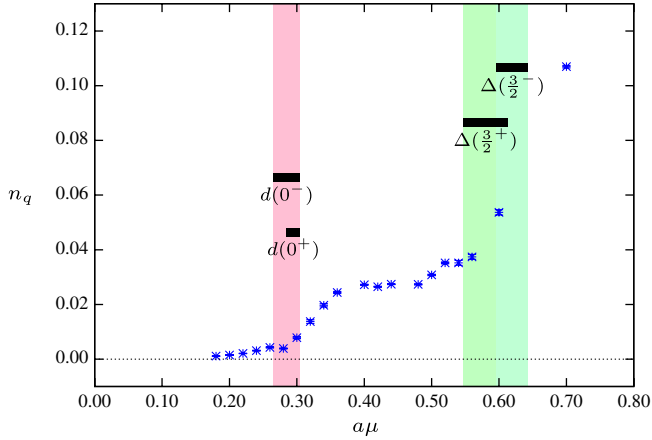
FIG. 9 (color online). Shown is the quark number density compared to baryon mass divided by baryon number for the heavy ensemble.
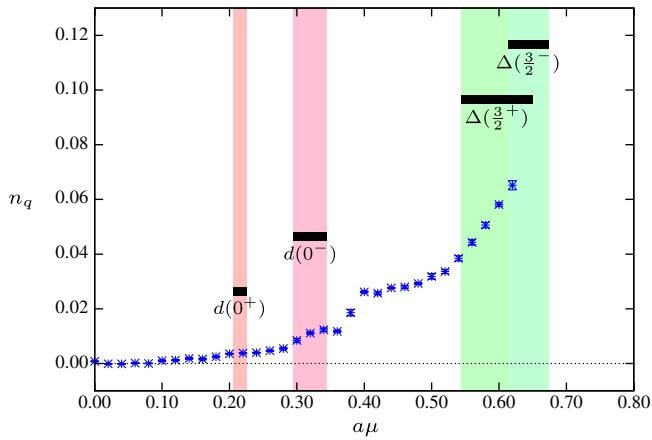

FIG. 10 (color online). Shown is the quark number density compared to baryon mass divided by baryon number for the light ensemble.

It is quite interesting to compare these transitions to the masses of the diquarks and baryons normalized by their baryon number.

For the heavy ensemble, in addition to the silver blaze transition due to the diquark states we find good agreement of the Δ mass with the point where the quark number density increases without building a plateau.

For the light ensemble the two transitions at $a\mu \approx 0.22$ and $a\mu \approx 0.32$, each followed by a plateau (see Fig. 10), can be related to the observation of the splitting of the 0^+ and 0^- diquark masses. Again the transition at $a\mu \approx 0.55$ is in good agreement with the Δ mass divided by 3.

For both ensembles our observation is thus that transitions in the quark number density approximately coincide with various hadron masses divided by their baryon number. For a bosonic hadron a plateau is formed after the transition, while for a fermionic hadron the quark number density increases further with increasing chemical

potential. In both ensembles we observe also a transition at $a\mu \approx 0.52$ (heavy ensemble) and $a\mu \approx 0.38$ (light ensemble) that does not coincide with any of our spectroscopic states. Since this transition is followed by a plateau we speculate that this state might also be a bosonic hadron. A possible candidate could for example be a bound state of four quarks. However, this may also relate to some of the known states, if their masses turn out to be significantly dependent on the chemical potential. It is also possible that additional collective excitations arise if any of the phases sustain a Bose-Einstein condensate, as has been argued for the low-density phase in two-color QCD [17–23].

This question is not simple to decide, as it is not clear how to reliably and unambiguously determine the mass of (quasi) particles at finite density in lattice simulations. However, it will be crucial to understand it in the future.

C. Free fermions

Further interesting insights can be gained by comparing the results with the corresponding ones for noninteracting systems of fermionic particles. On the one hand, this can test whether the idea of (quasifree) fermions or fermionic quasiparticles describe the theory adequately at some densities. On the other hand, the saturation effects should also yield a quasifree behavior, indicating the onset of lattice artifacts. We will only consider here the heavy ensemble, as for the light ensemble the acceptance rate dropped seriously in the range of $a\mu = 0.7$ to $a\mu \approx 1.5$, and therefore we cannot really assess the intermediate and saturation regime yet.

We begin with the fermion density for a theory of free lattice (Wilson) fermions with mass $\tilde{m} = m + d = 1/(2\kappa)$. It can be derived in analogy to the staggered result of [18] and is given by

$$n_f^{\text{free}}(\mu, \tilde{m})/n_f^{\text{sat}} = \sum_{\tilde{p}} \frac{2i\sqrt{1 - \tilde{p}_0^2}(\sum_i \tilde{p}_i - \tilde{m})}{4 + \tilde{m}^2 - 2\tilde{m}\sum_\mu \tilde{p}_\mu(\sum_{\nu > \mu} \tilde{p}_\nu - \tilde{m})}$$

(43)

where the sum extends over all lattice momenta

$$\tilde{p}_0 = \cos\left(\frac{2\pi}{N_t}\left(k_0 + \frac{1}{2}\right) - i\mu\right) \quad \text{and}$$

$$\tilde{p}_i = \cos\left(\frac{2\pi k_i}{N_s}\right) \quad \text{with}$$

$$k_0 = 1\ldots N_t \quad \text{and} \quad k_i = 1\ldots N_s. \quad (44)$$

When we tried to fit our data for the heavy ensemble to this formula with fitting parameters κ (which enters $\tilde{m}$) and n_f^{sat} we observed that the behavior changes at around $a\mu \approx 1$, see Fig. 11. Above $a\mu = 1$ the best fit for the data yields $\kappa = 0.162$ and $n_f^{\text{sat}} = 14.4$. This is in good agreement with the values for free quarks of $\kappa = 0.147$ and
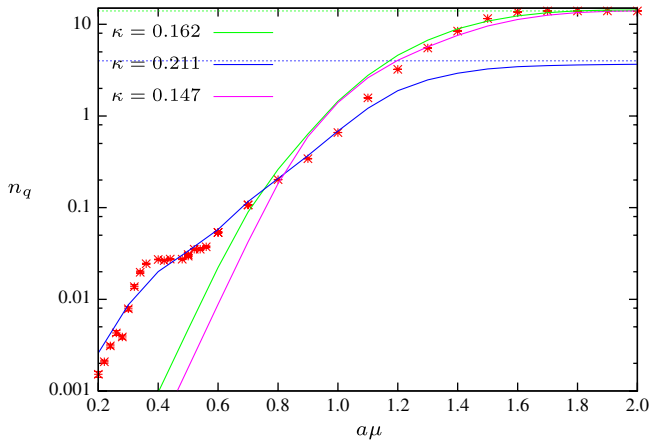
FIG. 11 (color online).   Fit of the quark number density for the heavy ensemble with the density for free lattice fermions.

$n_f^{sat} = n_q^{sat} = 14$. Although we expect that for very large values of μ the theory is exactly described by free quarks, in this intermediate region the Polyakov loop is not constant, and also the contribution of gluons to the free energy has not yet reached its quenched limit [29]. This might explain deviations from the exact values. Still, the rather good fit suggests strongly that for $a\mu > 1$ lattice artifacts become important.

Below $a\mu = 1$ the data are very well described by $\kappa = 0.211$ and $n_f^{sat} = 4.02$. The theoretical value for the saturation of a lattice gas of free Δ baryons is $n_B^{sat} = 4$. This suggests that between $a\mu \approx 0.6$ and $a\mu \approx 1.0$ the main contribution to the quark number density may come from fermionic baryons, in agreement with our findings in the last section. Somewhat surprisingly these fermionic baryons would behave very much like a noninteracting gas. One should note, however, that formally the κ value yields a negative mass. This is a consequence of using Wilson fermions. In principle we would have to correct for the additive mass shift. However, we do not yet know $\kappa_{critical}$ to do so. Determining it will require substantial amounts of calculation time, currently beyond our reach.

VII. CONCLUSIONS

We have presented a first study of the hadronic spectrum of G_2-QCD. We found that for sufficiently small quark masses a splitting of the spectrum is observed into a Goldstone sector, an intermediate bosonic sector, and a nucleonic sector, quite similar to the situation in ordinary QCD. The spectrum also shows strong evidence of spontaneous chiral symmetry breaking, like the emergence of the aforementioned Goldstone bosons, or the nondegeneracy of parity partners. Therefore, the hadronic physics appears to be qualitatively similar to QCD, even though there are many more states in the spectrum. Unfortunately we could not reliably determine the mass of the lightest hybrid, though this would be crucial in assuring that the nucleon dynamics is truly similar to QCD. This will require a much more sophisticated spectroscopy analysis in the future.

We have also found evidence that the scale hierarchy of the vacuum reflects itself in the phase structure at finite densities. We found a number of transitions, in particular for light quark mass, which correlate with the scales of the hadron spectrum. In fact, we even found an additional transition. This already indicates a very rich phase structure of the theory at finite densities. We also find some hints that a phase dominated by fermionic hadrons may exist at quark chemical potentials of about 300–600 MeV.

Besides understanding in more detail the already observed phase structure, the next logical step is to go to smaller lattice spacings and larger lattices. This would ensure that we can disentangle the transition occurring at the nucleon scale from possible lattice artifacts. Also, larger volumes will be necessary to reduce artifacts from the residual temperature. Both steps are necessary to show whether a genuine nuclear matter phase is present, which would be of central importance for a qualitative understanding of fermionic effects in finite density QCD and, eventually, neutron stars.

[1] S. Leupold, C. Höhne, J. Knoll, S. Leupold, J. Randrup, R. Rapp, and P. Senger, Lect. Notes Phys. **814**, 39 (2011).

[2] P. Braun-Munzinger and J. Wambach, Rev. Mod. Phys. **81**, 1031 (2009).

[3] C. Gattringer and C. B. Lang, Lect. Notes Phys. **788**, 1 (2010).

[4] P. de Forcrand, *Proc. Sci.* LAT2009 (**2009**) 010.

[5] O. Philipsen, Acta Phys. Pol. B Proc. Suppl. **5**, 825 (2012).

[6] M. Buballa, Phys. Rep. **407**, 205 (2005).

[7] J. M. Pawlowski, AIP Conf. Proc. **1343**, 75 (2011).

[8] J. Braun, J. Phys. G **39**, 033001 (2012).

[9] C. Bonati, P. de Forcrand, M. D'Elia, O. Philipsen, and F. Sanfilippo, *Proc. Sci.* LATTICE2011 (**2011**) 189.

[10] P. de Forcrand and O. Philipsen, Phys. Rev. Lett. **105**, 152001 (2010).

[11] P. Cea, L. Cosmai, M. D'Elia, A. Papa, and F. Sanfilippo, Phys. Rev. D **85**, 094512 (2012).

[12] J. Kogut and D. Sinclair, Phys. Rev. D **70**, 094501 (2004).

[13] P. de Forcrand, M. A. Stephanov, and U. Wenger, *Proc. Sci.* LAT2007 (**2007**) 237.

[14] M. Fromm, J. Langelage, S. Lottini, and O. Philipsen, J. High Energy Phys. 01 (2012) 042.

[15] M. Fromm, J. Langelage, S. Lottini, M. Neuman, and O. Philipsen, Phys. Rev. Lett. **110**, 122001 (2013).

[16] D. Sexty, arXiv:1307.7748.

[17] J. Kogut, M. A. Stephanov, D. Toublan, J. Verbaarschot, and A. Zhitnitsky, Nucl. Phys. **B582**, 477 (2000).

[18] S. Hands, I. Montvay, S. Morrison, M. Oevers, L. Scorzato, and J. Skullerud, Eur. Phys. J. C **17**, 285 (2000).

[19] S. Hands, S. Kim, and J.-I. Skullerud, Eur. Phys. J. C **48**, 193 (2006).

[20] S. Hands, P. Kenny, S. Kim, and J.-I. Skullerud, Eur. Phys. J. A **47**, 60 (2011).

[21] N. Strodthoff, B.-J. Schaefer, and L. von Smekal, Phys. Rev. D **85**, 074007 (2012).

[22] N. Strodthoff and L. von Smekal, arXiv:1306.2897.

[23] T. Boz, S. Cotter, L. Fister, D. Mehta, and J.-I. Skullerud, Eur. Phys. J. A **49**, 87 (2013).

[24] F. Karsch and M. Lutgemeier, Nucl. Phys. **B550**, 449 (1999).

[25] J. Engels, S. Holtmann, and T. Schulze, Nucl. Phys. **B724**, 357 (2005).

[26] E. Bilgici, C. Gattringer, E.-M. Ilgenfritz, and A. Maas, J. High Energy Phys. 11 (2009) 035.

[27] J. Danzer, C. Gattringer, and A. Maas, J. High Energy Phys. 01 (2009) 024.

[28] K. Holland, P. Minkowski, M. Pepe, and U. J. Wiese, Nucl. Phys. **B668**, 207 (2003).

[29] A. Maas, L. von Smekal, B. Wellegehausen, and A. Wipf, Phys. Rev. D **86**, 111901 (2012).

[30] A. Maas and B. H. Wellegehausen, *Proc. Sci.* LAT-TICE2012 (**2012**) 080.

[31] A. Borowiec, J. Lukierski, V. Lyakhovsky, M. Mozrzymas, and V. N. Tolstoy, J. Math. Phys. (N.Y.) **46**, 103502 (2005).

[32] A. Macfarlane, Int. J. Mod. Phys. A **17**, 2595 (2002).

[33] I. Yokota, arXiv:0902.0431.

[34] M. Pepe and U. J. Wiese, Nucl. Phys. **B768**, 21 (2007).

[35] B. H. Wellegehausen, A. Wipf, and C. Wozar, Phys. Rev. D **83**, 114502 (2011).

[36] A. Maas and Š. Olejník, J. High Energy Phys. 02 (2008) 070.

[37] S. L. Cacciatori, B. L. Cerchiai, A. D. Vedova, G. Ortenzi, and A. Scotti, J. Math. Phys. (N.Y.) **46**, 083512 (2005).

[38] J. Greensite, K. Langfeld, S. Olejnik, H. Reinhardt, and T. Tok, Phys. Rev. D **75**, 034501 (2007).

[39] G. P. Engel, C. Lang, M. Limmer, D. Mohler, and A. Schafer (BGR [Bern-Graz-Regensburg] Collaboration), Phys. Rev. D **82**, 034505 (2010).

[40] S. Duane, A. D. Kennedy, B. J. Pendleton, and D. Roweth, Phys. Lett. B **195**, 216 (1987).

[41] K. Symanzik, Nucl. Phys. **B226**, 187 (1983).

[42] K. Symanzik, Nucl. Phys. **B226**, 205 (1983).

[43] M. Lüscher and P. Weisz, Commun. Math. Phys. **97**, 59 (1985).

[44] R. Horsley, H. Perlt, P. E. L. Rakow, G. Schierholz, and A. Schiller, Phys. Rev. D **78**, 054504 (2008).

[45] A. Kennedy, I. Horvath, and S. Sint, Nucl. Phys. B, Proc. Suppl. **73**, 834 (1999).

[46] D. Weingarten and D. Petcher, Phys. Lett. **99B**, 333 (1981).

[47] W. Fraser, J. Assoc. Comput. Mach. **12**, 295 (1965).

[48] B. Jegerlehner, arXiv:hep-lat/9612014.

[49] R. D. Ruth, IEEE Trans. Nucl. Sci. **30**, 2669 (1983).

[50] J. Sexton and D. Weingarten, Nucl. Phys. **B380**, 665 (1992).

[51] T. Takaishi and P. de Forcrand, Phys. Rev. E **73**, 036706 (2006).

[52] H. Yoshida, Phys. Lett. A **150**, 262 (1990).

[53] K. Jansen, A. Shindler, C. Urbach, and U. Wenger, *Proc. Sci.* LAT2005 (**2006**) 118.

[54] C. Allton, C. Sachrajda, R. Baxter, S. Booth, K. Bowler, S. Collins, D. Henty, R. Kenway, C. McNeile, B. Pendleton, D. Richards, J. Simone, A. Simpson, A. McKerrell, C. Michael, and M. Prisznyak, Nucl. Phys. **B407**, 331 (1993).

[55] M. Clark and A. Kennedy, Nucl. Phys. B, Proc. Suppl. **140**, 838 (2005).

[56] S.-J. Dong and K.-F. Liu, Phys. Lett. B **328**, 130 (1994).

[57] K. Bitar, A. Kennedy, R. Horsley, S. Meyer, and P. Rossi, Nucl. Phys. **B313**, 348 (1989).

[58] G. Cossu, M. D'Elia, A. D. Giacomo, B. Lucini, and C. Pica, J. High Energy Phys. 10 (2007) 100.

[59] T. D. Cohen, Phys. Rev. Lett. **91**, 222001 (2003).